Multi-grid 3D-OSEM reconstruction technique for high resolution rotating-head PET scanners

Juan E. Ortuño, José L. Rubio, Pedro Guerra, *Student Member, IEEE*, George Kontaxakis, *Senior Member, IEEE*, and Andrés Santos, *Senior Member, IEEE*

***Abstract*– A fast statistical iterative image reconstruction algorithm has been developed for high resolution PET scanners based on rotating plane detectors. The proposed technique consists of a multi-grid version of the 3D ordered subsets expectation-maximization (3D-OSEM) algorithm. The associated system matrix is precalculated for the fine grid resolution with Monte Carlo methods. Coarse grid system matrices and subset subdivision are derived at a post-process step. Only the system matrix elements associated to the fourth part of central transverse planes are stored in sparse mode format, using axial and in-plane transaxial symmetries during the reconstruction. The multi-grid proposed technique has been evaluated on 3D sinograms obtained from GATE simulations, reporting better resolution-noise trade-off than SSRB+2D-OSEM and FORE+2D-OSEM algorithms, specially in the axial direction and far from the center of the FOV. The proposed algorithm shows significantly faster convergence rate than single-grid 3D-OSEM when is applied to images with local smoothness property.**

I. Introduction

THE MLEM algorithm (maximum-likelihood expectation-maximization) [1] is a powerful image reconstruction technique widely employed in PET imaging. Because of the low geometric sensitivity and the required high spatial resolution, 3D versions of the MLEM algorithm are well suited for small animal planar-head, rotating PET cameras.

The ordered subsets expectation-maximization (OSEM) algorithm [2] (a block sequential version of the MLEM algorithm) accelerates MLEM and is commonly employed in commercial and experimental PET cameras. In this work we study a novel iterative algorithm that combines the 3D-OSEM with the multi-grid expectation maximization (MGEM) algorithm [3], which is based on the idea that low image frequencies can converge faster than the high frequency ones. The MGEM algorithm is initialized with a coarse grid, where the low frequency components are recovered in fast iterations due to the smaller dimensionality of the coarse grid system matrix. When near convergence, the resulting image is interpolated onto the next finer grid.

The image quality depends on the accurate modeling of the system matrix: i.e., the set of a priori probabilities that an event generated in a voxel i is detected in the line of response (LOR) j, $\{p_{ij}\}$. Practical implementation at reasonable times however imposes the use of approximations where the majority of p_{ij} have zero or negligible values. Efficient sparse-matrix storage and reading techniques can avoid the calculations of p_{ij} on the fly. In 3D case, the number of non-zero system matrix values is too large, and the pre-calculated system matrix must be compressed with the consideration of possible redundancies, i.e., axial and in-plane symmetries [4]. System matrix estimation can be performed by Monte Carlo methods than incorporate physical effects not included in an analytical model [5].

We have evaluated a multi-grid 3D-OSEM algorithm with precalculated system matrix, optimized to high resolution planar-head PET cameras composed of pixelated scintillator crystal arrays. The comparison with single-grid 2D-OSEM and single-grid 3D-OSEM has been also performed.

II. Materials and Methods

A. Scanner Geometry and Data Format

The simulated small animal PET scanner design used in this work consists of two pairs of planar detectors in coincidence mode, with 160 mm of separation between opposite detectors. Each detector is composed of a 30×35 array of 1.5×1.5×12 mm^3 LYSO pixelated crystals, assembled on a 100 μm thick matrix of plastic reflector. The detectors are mounted on a rotating gantry with 180º rotation span [6]. A schematic of the scanner's configuration is plotted in the fig. 1.

The coincidences associated to the pixelated crystals located in the detector extremes are not used in the reconstruction process, and the useful field of view (FOV) completely covered by the detectors is 44.8×44.8×56 mm^3.

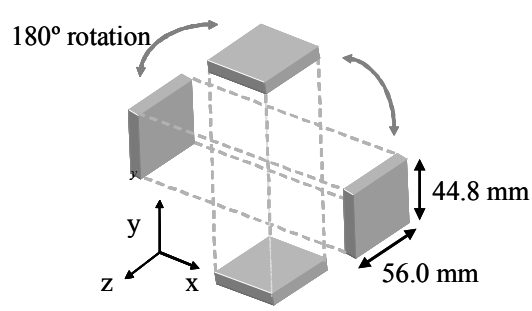

Fig. 1. Scheme of the scanner geometry employed in this work: Two pairs of planar detectors composed of pixelated crystals and mounted on a rotating gantry.

Coincidences are binned in direct and oblique sinograms as a function of four variables: (s, φ, θ, r), where s is the distance

Manuscript received November 15, 2006. This work has been partly funded by the Spanish Ministry of Health (PI052204), the Spanish Ministry of Education and Science (TEC2004-0752-C02-02) and by the CDTEAM project of the Spanish Ministry of Industry.

The authors are with the Electronic Engineering Department (DIE) of the E.T.S.I Telecomunicación, Universidad Politécnica de Madrid, Spain (fax: (+34-91-336-73-23, e-mail: juanen@die.upm.es).

between the z axis and the LOR projection onto a transverse plane; φ is the LOR azimuthal angle; θ is the angle between the LOR and the transverse plane, and r is the mean between the axial coordinates of the two crystals in coincidence [7]. The following equations converts the absolute coordinates of the two crystals involved in coincidence, (x_1,y_1,z_1) and (x_2,y_2,z_2), into the 3D sinogram parameters:

$$s=\sqrt{x_1^2+y_1^2}\,\sin\left(\arctan\left(\frac{y_1}{x_1}\right)-\varphi\right) \qquad \varphi=\arctan\left(\frac{y_2-y_1}{x_2-x_1}\right)$$

$$\theta=\arctan\left(\frac{z_2-z_1}{\sqrt{(x_2-x_1)^2+(y_2-y_1)^2}}\right) \qquad r\simeq\frac{z_1+z_2}{2}$$

Sampled values are obtained for s and φ with nearest-neighbor interpolation, while θ and r are mapped onto z_1 and z_2 using linear interpolation.

This parametrization is also employed in the system matrix pre-calculation, where the non-zero sinogram bins (i.e., scaled probabilities p_{ij}) are assigned to the corresponding subset and stored in sparse matrix format.

B. System Matrix and Symmetries

We consider a 3D discretized PET model, where the field of view (FOV) is divided in cuboid-shaped regions (voxels) in which the activity is assumed to be constant.

The system matrix must be precalculated using only once when a design parameter is modified (voxel size, crystal number, rotating span). The simulation details, using Monte Carlo Methods, have been previously described [8], and include attenuation and scatter effects in the detector. In the multi-grid scheme, system matrix simulation is performed only for the finest grid, with voxels without overlap. The finest grid voxel size is chosen at one quarter the size of the pixelated crystal, to ensure that the intrinsic scanner resolution is maintained (both in the transaxial plane and the axial axis).Coarse grids can be computed joining neighboring voxels of the highest order level grid.

Two different axial alignments have been modeled (figs. 2 and 3), which allow to obtain p_{ij} for other parallel LORs, by translation of the voxel coordinates along z. The parallel shift redundancies applied are (fig. 4.):

$$z_p \rightarrow z_p + nN_d, \quad z_{d1} \rightarrow z_{d1} + N_d, \quad z_{d2} \rightarrow z_{d2} + N_d$$

where z_p is z coordinate index of voxel in the range $[0,N_z)$, z_{d1} and z_{d2} are the pixelated crystal row indexes associated to the coincidence, N_d is the axial shift (in units of number of crystals), and n denotes the number of slices that match the crystal thickness in the z dimension.

Analogous, the reflection symmetry along the axial direction (fig. 4) obtain p_{ij} for symmetric LORs, and is expressed as:

$$z_p \rightarrow nN_z - z_p, \quad z_{d1} \rightarrow N_z - 1 - z_{d1}, \quad z_{d2} \rightarrow N_z - 1 - z_{d2}$$

With the axial alignment proposed in fig. 2, only two central slices need to be modeled in detail for the finest resolution (n=4), while the rest of the slices are obtained with reflection axial symmetry and parallel shift axial redundancies. The alignment proposed in fig. 3 requires the simulation of at least three slices. In both alignments, coarse grids involve voxel sizes half or exactly the size of the pixelated crystal in the z dimension, but only the alignment of fig. 2 can pre-compute the system matrix probabilities by joining voxels of the finest grid.

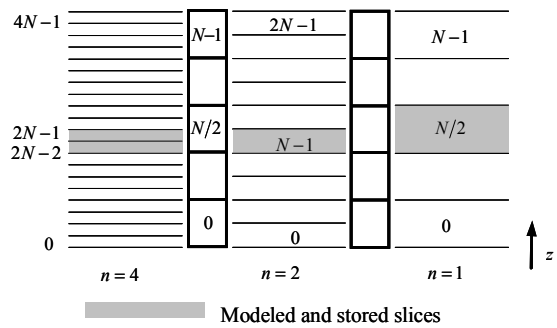

Fig. 2. The number of modeled transaxial slices depends of the thickness and alignment of the voxel grid. With the axial alignment plotted in this figure, only two central slices need to be modeled in detail for the finest grid.

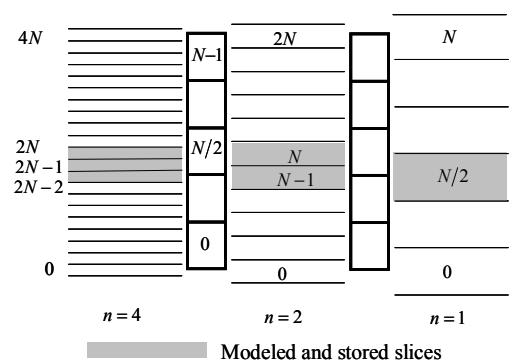

Fig. 3. In this axial alignment of the voxel grid, at least three slices need to be modeled to obtain the rest of the slices with symmetries.

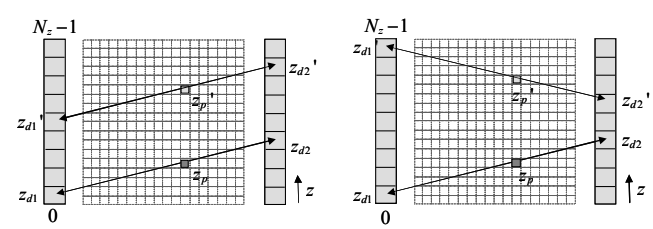

Fig. 4. Parallel shift (left) and axial symmetry (right) along the axial direction (z). LORs belonging to voxels z'_p derivates from LORs from z_p.

Since scanner demostrates rotational symmetry, in-plane symmetries have been used, modeling only the voxels belonging to the first quadrant. One voxel i_1 with (k,l) transaxial indexes has the following in-plane rotational symmetry relationship with voxels i_2, i_3 and i_4 (fig. 5):

$$i_1 \rightarrow i_2 \;\Rightarrow \varphi \rightarrow (\varphi + \pi)$$
$$i_1 \rightarrow i_3 \;\Rightarrow \varphi \rightarrow (\varphi - \pi/2)$$
$$i_1 \rightarrow i_4 \;\Rightarrow \varphi \rightarrow (\varphi + \pi/2)$$

During the projection and backprojection steps, the stored p_{ij} values are sequentially read with their [s, φ] and [θ, r] associated positions. Since the axial symmetries involve a change of θ and r values, a lookup-table provides the new [s, φ, θ', r'] values related to voxels in the same x-y position and different transverse planes. On the other hand, in-plane symmetries shift φ values by a multiple of 90º.

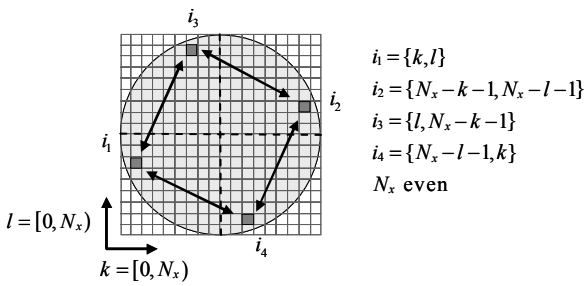

Fig. 5. Only the fourth part of voxels belonging to one transaxial slice are stored in the pre-calculated system matrix, obtaining the rest by rotational symmetry.

III. Experiments and Results

35^2 oblique sinograms of 55×120 bins are formed from the collected list-mode data respecting the resolution limits of the system. The data are divided in 10 subsets and a LOR is assigned to subset $n = mod\ (\varphi,\ 10)$, balanced according to the azimuthal angle φ. Three grid levels are used, from the coarser of 28×28×35 voxels, to the finest of 112×112×140 voxels. The sinogram size is kept constant in the multi-grid scheme. The precalculated system matrix parameters are represented in table 1.

Image Size (x,y,z)	SM elements	Size of stored values (MB)	Nº of stored voxels	SM elements by stored voxel	Sparsity in stored voxels
28×28×35	2.22×10^{11}	41.24	152	83416	98.969%
28×28×36	2.28×10^{11}	76.86	304	77703	99.039%
56×56×70	1.77×10^{12}	95.88	612	48140	99.405%
56×56×71	1.80×10^{12}	192.51	1224	48329	99.402%
112×112×70	7.10×10^{12}	301.16	2454	37713	99.534%
112×112×71	7.20×10^{12}	637.18	4908	39902	99.507%
112×112×140	1.42×10^{13}	596.13	4098	37324	99.538%
112×112×141	1.43×10^{13}	895.86	7362	37394	99.537%

Table 1. Parameters of the precalculated system matrix (SM) set. The sinogram size is 55×120×35×35.

The multi-grid 3D-OSEM scheme was evaluated with realistic phantom simulations performed with GATE [9]. A 12 ns time-coincidence window and 0.4-0.7 MeV energy window have been used. 15 point sources were placed in a warm cylinder (20 mm radius by 48 mm length) to quantify the noise and resolution properties. The radial positions were located at r={2,6,10,14,18} mm off-center, in three transverse planes z={-20,0,10} mm. The generated events in the point sources were 1/5 times the events of the cylinder and 14 million coincidences were collected. A multi-grid 3D-OSEM reconstructed image of this study is shown in fig. 6.

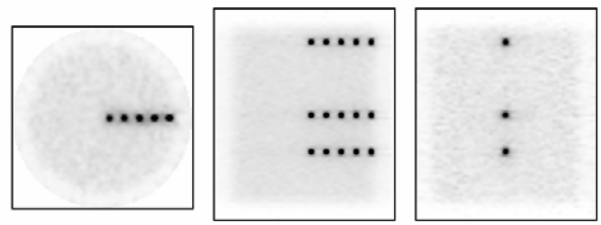

Fig. 6. Multi-grid 3D-OSEM reconstruction of point sources in a warm cylinder simulated with GATE. Transverse, saggital and coronal sections.

In fig. 7, the geometric mean of the radial, tangential and axial resolution (specified by the FWHM of the adjusted Gaussian curve), of point sources located on the central transverse plane is plotted against the radial position. The methods compared are SSRB+2D-OSEM (single slice rebinning followed by 2D-OSEM), FORE+2D-OSEM (Fourier rebinning), multi-grid and single-grid 3D+OSEM. 5 iterations and 10 subsets were used in all cases. The maximum axial rebinning for 2D methods was chosen 15 and 25 pixelated crystals.

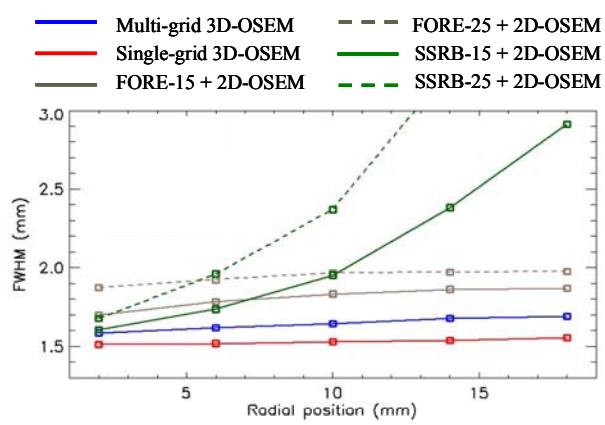

Fig. 7. 2D-OSEM and 3D-OSEM resolution vs. radial position figure.

Noise-resolution curves are plotted in fig. 8. The number of iterations is referred to the finest grid iterations. The coefficient of variation (COV) is defined as the standard deviation divided by the mean, and is measured on the warm cylinder, over 500 random selected voxels per slice. The resolution (FWHM) is referred to the mean value for point sources in the central transverse plane.

These results show a better resolution-noise trade-off than SSRB+2D-OSEM and FORE+2D-OSEM methods, especially

far from the center of the FOV, while converging faster than single-grid 3D-OSEM.

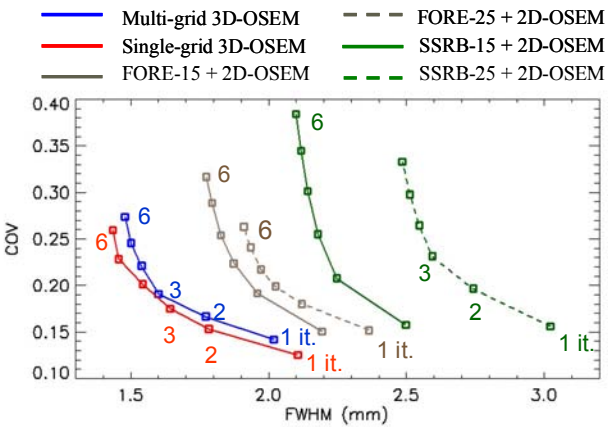

Fig. 8. 2D-OSEM and 3D-OSEM noise vs. resolution figure.

A Derenzo-type phantom was simulated with GATE, with a total amount of 4.8 millions of coincidences, and water-filled rods of {4.8, 3.6, 2.4, 1.8, 1.2} mm diameter, with the same distance between surfaces. In fig. 9, transverse central planes are shown for multi-grid and single-grid 3D-OSEM. Reconstructions times in each iteration vary from 12min 56s for the finest grid to 21s (see table 2), for the coarsest grid, improving the total reconstruction time in the multi-grid scheme with the same number of total iterations.

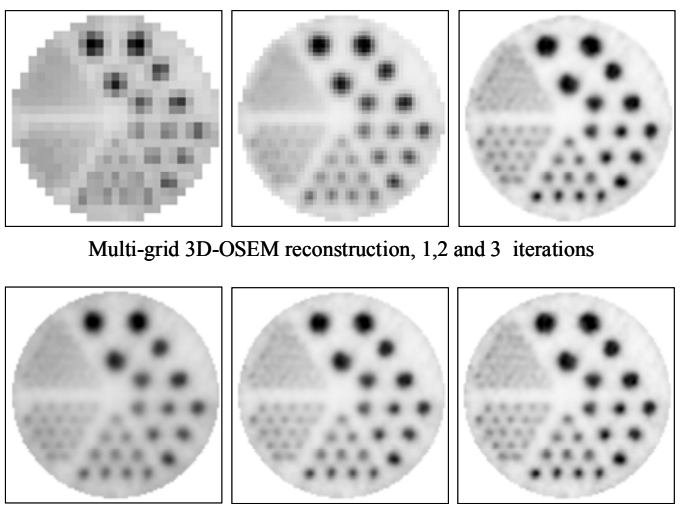

Fig. 9. Derenzo-type GATE simulation. Up: multi-grid 3D-OSEM (3 iterations with different grids). Bottom: single-grid 3D-OSEM reconstruction (1,2 and 3 iterations).

Image Size	28x28x35	56x56x70	112x112x70	112x112x140
Rec. time	21s	1min30s	4min40s	12min56s
Image Size	28x28x36	56x56x71	112x112x71	112x112x141
Rec. time	33s	2min17s	7min33s	16min47s

Table 2. Computing time for one iteration over 10 subsets, for different image sizes employed the multi-grid scheme. (PC Pentium IV, 3.2 MHz CPU clock and 1GB RAM)

IV. Conclusions

A fast multi-grid 3D-OSEM iterative image reconstruction scheme has been implemented and evaluated for high resolution planar-head rotating small animal PET cameras. The algorithm employs pre-calculated system matrix, simulated with Monte Carlo methods and stored in an efficient way in sparse matrix format. The reconstruction of simulations performed with GATE have reported better resolution/noise curves than the 2D-OSEM algorithm, whereas the convergence is accelerated with respect to the equivalent single-grid method without appreciable loss of image quality. The accelerating technique of MLEM provides a good trade-off between quality and reconstruction time.

Acknowledgment

The authors wish to thank J.J Vaquero and M. Desco, from the G.U Gregorio Marañón Hospital (Madrid, Spain) for motivation, discussion and comments.

V. References

[1] L. A. Shepp and Y. Vardi, "Maximum likelihood reconstruction in positron emission tomography," *IEEE Trans. Med. Imag.*, vol. 1, pp. 113-122, Oct. 1982.

[2] H. M. Hudson and R. S. Larkin, "Accelerated image-reconstruction using ordered subsets of projection data," *IEEE Trans. Med. Imag.*, vol. 13, pp. 601-609, Dec. 1994.

[3] M. V. Ranganath, A. P. Dhawan, and N. Mullani, "A Multigrid Expectation Maximization Reconstruction Algorithm for Positron Emission Tomography," *IEEE Trans. Med. Imag*, vol. 7, pp. 273-278, Dec. 1988.

[4] C. A. Johnson, Y. C. Yan, R. E. Carson, R. L. Martino, and M. E. Daube-Witherspoon, "A system for the 3D reconstruction of retracted-septa PET data using the EM algorithm," *IEEE Trans. Nuc. Sci.*, vol. 42, pp. 1223-1227, Aug. 1995.

[5] J. Y. Qi, R. M. Leahy, S. R. Cherry, A. Chatziioannou, and T. H. Farquhar, "High-resolution 3D Bayesian image reconstruction using the microPET small-animal scanner," *Phys. Med. Biol.*, vol. 43, pp. 1001-1013, Apr 1998.

[6] J. J. Vaquero, E. Lage, L. Ricón, M. Abella, E. Vicente, and M. Desco, "rPET Detectors Design and Data Processing," *Nuclear Science Symposium Conference Record*, vol 5, pp. 2885-2889. Oct. 2005.

[7] M. Defrise, P. E. Kinahan, D. W. Townsend, C. Michel, M. Sibomana, and D. Newport, "Exact and approximate rebinning algorithms for 3-D PET data," *IEEE Trans. Med. Imag.*, vol. 16, pp. 145-158, April 1997.

[8] J. E. Ortuño, P. Guerra, J. L. Rubio, G. Kontaxakis, and A. Santos, "3D OSEM-Based Iterative Image Reconstruction for High Resolution PET Using Precalculated System Matrix," *Nucl. Instrum. Meth. A.*, In Press.

[9] S. Jan, G. Santin, D. Strul, S. Staelens, et al., "GATE: a simulation toolkit for PET and SPECT," *Phys. Med. Biol.*, vol. 49, pp. 4543-4561, Oct. 2004.